Received 15 April 2021; revised 25 May 2021; accepted 13 June 2021. Date of publication 16 June 2021; date of current version 24 June 2021.

Digital Object Identifier 10.1109/OJCOMS.2021.3089690

Continuous-Phase Modulation for DFT-Spread Localized OFDM

JEONGHOON CHOI [1], JOON HO CHO [1] (Member, IEEE), AND JAMES S. LEHNERT [2] (Fellow, IEEE)

[1]Department of Electrical Engineering, Pohang University of Science and Technology, Pohang 37673, South Korea

[2]School of Electrical and Computer Engineering, Purdue University, West Lafayette, IN 47907, USA

CORRESPONDING AUTHOR: J. H. CHO (e-mail: jcho@postech.ac.kr)

This work was supported in part by the Institute for Information and Communications Technology Promotion (IITP) through grant funded by MSIT of the Korea Government under Grant 2021(2016-0-00123), and in part by the National Research Foundation Grant from the Ministry of Education for Basic Science Research Program under Grant 2018R1D1A1A02086169 (QAM-FBMC: New Waveform Design for 6G & Beyond Mobile Communication Standards).

ABSTRACT Massive machine-type communications to support a large number of low-cost, low-power, and/or low-rate radio-frequency transceivers such as Internet-of-Things (IoT) devices is a major usage scenario of the 5G mobile communication system. To save cost and power, highly nonlinear power amplifiers (PAs) are expected to be used in the devices. However, the envelope fluctuation of the input of a PA may make the output suffer from severe nonlinear distortion. In this paper, a continuous-phase modulation is proposed for discrete-Fourier transform (DFT)-spread localized orthogonal frequency-division multiplexing (OFDM) of $\pi/2$-BPSK symbols. In particular, the combination of a spectrum shaping vector and an extra rotation angle is proposed, which enables the use of a receiver that is fully compatible with the current standard. It is shown that the proposed design significantly outperforms the conventional designs in terms of effective signal-to-distortion ratio and error vector magnitude at the cost of a negligible increase in out-of-band emission.

INDEX TERMS Continuous-phase modulation, constellation rotation, DFT-spread OFDM, nonlinear power amplifier, minimum-shift keying, pulse shaping.

I. INTRODUCTION

THE 5TH generation (5G) New Radio (NR) mobile communications has three major usage scenarios [1]. Among them, enhanced mobile broadband and ultra-reliable low-latency communications scenarios mainly focus on the improvement of the performance metrics such as the bit-error rate, throughput, and latency. The massive machine type communications (mMTC) scenario, however, has a different set of design requirements, because its objective is to support the connectivity of a large number of low-cost, low-power, and/or low-rate radio-frequency (RF) transceivers [2]–[4]. Much effort is currently being made, e.g., during the meetings of the 3rd Generation Partnership Project to fully support the mMTC scenario with the NR or next generation standards.

To save cost and power, it is expected that a transmitter (TX) of an Internet-of-Things (IoT) device, such as a machine-embedded sensor, is equipped with a nonlinear power amplifier (PA). However, severe nonlinear distortion cannot be avoided unless the input of the PA is close to a continuous-phase modulation (CPM) signal that has a constant envelope [2]. The objective of this paper is to propose a transmission method that makes the input signal an almost constant-envelope (CE) signal and, at the same time, enables the use of a receiver (RX) that is fully compatible with the uplink of the current 4th generation (4G) Long-Term Evolution (LTE) and 5G NR standards based on orthogonal frequency-division multiplexing (OFDM).

OFDM-related modulation methods for generating almost CE signals have been investigated in [5]–[10]. In [5] and [6], CE-OFDM methods are proposed, where a discrete multitone (DMT) modulator [11], [12] and a discrete-Fourier transform (DFT)-spread OFDM modulator, respectively, are used with phase modulators. Although the TXs generate almost CE signals, these transmission methods are not compatible with the uplink of the current standards. This

is because the DMT modulator and DFT-spread OFDM modulator are employed, respectively, in [5] and [6] just as the pre-coders of the nonlinear phase modulators at the TXs. Moreover, after phase demodulation at the RXs, linear communication channels now look nonlinear to the DMT and DFT-spread OFDM signals. Hence, conventional one-tap frequency-domain equalizers (FDEs) developed for OFDM RXs cannot recover the orthogonality among the sub-carriers in frequency-selective channels [7].

In [7], CPM single-carrier frequency-division multiple-access (SC-FDMA) is proposed, where a sampled CPM signal is fed to a DFT-spread OFDM modulator. Unlike the work in [5], [6], a conventional low-complexity FDE can be used at the RX because the CPM modulator is just a pre-coder of the DFT-spread OFDM modulator. However, the CPM-SC-FDMA is not compatible with the standards, either. This is because the standards assign consecutive sub-carriers for localized OFDM (L-OFDM) [13], [14], while the CPM-SC-FDMA must assign non-consecutive equally-spaced sub-carriers for interleaved OFDM (I-OFDM).

In [8] and [9], time-domain (TD) implementation of the frequency-domain spectrum shaping (FDSS) is proposed for the DFT-spread L-OFDM of $\pi/2$-BPSK symbols with various combinations of a number of taps and tap weights. This method filters $\pi/2$-BPSK symbols before the DFT spreading to reduce the peak-to-average power ratio (PAPR) and is fully compatible with the standards. As will be shown in Section IV, the 6-tap and 3-tap TD shaping filters in [8] and [9], respectively, can achieve a PAPR of 1.5 dB and 2.4 dB for the same conditions. Unlike the PAPR measured at the input of a nonlinear PA, the error vector magnitude (EVM) measured at the output of a nonlinear PA is a more important performance metric to assess the average performance degradation due to the use of a nonlinear PA [15]. It will be shown that the TD filters exhibit high EVM when a highly nonlinear PA is chosen and a very small output back-off (OBO) is used for power-efficient operation of the PA.

In [10], motivated by the recent inclusion of the FDSS technique to the LTE and NR [16], a generalized FDSS is proposed for the DFT-spread L-OFDM of constellation-rotated BPSK symbols for future wireless systems. A numerically optimized FDSS vector, which can be viewed as a one-tap frequency-domain (FD) pre-equalizer, is shown to achieve an approximately 0.5 dB PAPR by using more sub-carriers than the number of $\pi/2$-BPSK symbols, i.e., by using excess sub-carriers. However, this method is not compatible with the standards in that, extra constellation rotation is needed by the RX. This method also requires the FDSS vector to be found through numerical search whenever a new combination of the numbers of $\pi/2$-BPSK symbols and excess sub-carriers is given.

In this paper, a CPM is proposed for DFT-spread L-OFDM to generate an almost CE signal and, at the same time, to enable the use of a RX that is fully compatible with the current standards. It is well known that a CPM signal can be written as a superposition of linearly modulated signals, where each signal has pseudo-symbols as data symbols and the Laurent functions as pulse shapes [17]–[20]. Among CPM signals, only a full-response binary CPM with modulation index $1/2$ allows the representation having a single linearly modulated signal. Moreover, among full-response binary CPM signals with modulation index $1/2$, the minimum-shift-keying (MSK) achieves the minimum frequency separation, when it is viewed as a binary continuous-phase frequency-shifted keying [11]. This property is desirable because the increase in the out-of-band (OOB) emission has to be minimized. Motivated by these facts, we modify the generalized FDSS technique with excess sub-carriers [10] in a way that a FD sampled MSK pulse is adopted as the FDSS vector. The modification includes an extra constellation-rotation at the TX but not at the RX for the compatibility with the current standard. Since the MSK pulse has a closed-form formula, unlike [10], no numerical optimization of the FDSS vector is needed for different combinations of the numbers of $\pi/2$-BPSK symbols and excess sub-carriers. The key assumption is that the bandwidth of an uplink transmit filter is much larger than the bandwidth of the transmitted signal. Fortunately, this assumption is often applied to the DFT-spread L-OFDM because the number and location of the assigned consecutive sub-carriers need to vary depending on how the resources are allocated [21]. It is shown, under this assumption, that the proposed method achieves near-zero dB PAPR and results in outstanding EVM at the output of a highly nonlinear PA with a very small OBO at the cost of a slight increase in OOB emission.

The rest of this paper is organized as follows. In Section II, the signal and system models are described. In Section III, the proposed combinations of an FDSS vector and an extra rotation angle are presented that generate almost CE signals. The properties of the proposed design are compared with those of conventional ones. Performance metrics and numerical results are presented in Section IV, and concluding remarks are offered in Section V.

II. SIGNAL AND SYSTEM MODELS

In this section, we describe the signal, TX, and RX models.

A. TRANSMITTER

It is assumed that a TX of an IoT device is assigned the $(K+1)$th to $(K+M)$th sub-carriers, where the first sub-carrier corresponds to the DC sub-carrier. We assume that M is an even number throughout this paper, as the standards have a multiple of 12 as M. Fig. 1 shows the block diagram of the TX in complex baseband.

In the first and second blocks, a sequence $(b_m)_{m\in\mathbb{Z}}$ of BPSK symbols is first converted to a sequence of length-M symbol vectors by a serial-to-parallel converter (S/P), where $b_m \in \{1, -1\}$. Without loss of generality, we consider the transmission of the first BPSK symbol vector denoted by $\boldsymbol{b}$. Then, $\boldsymbol{b}$ is pre-multiplied by the M-by-M diagonal phase-shift matrix

$$\boldsymbol{F} \triangleq \mathrm{diag}\{[1, \mathrm{j}, 1, \mathrm{j}, \ldots,]\}, \tag{1}$$

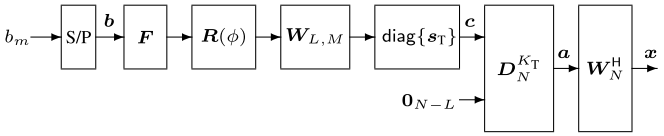

FIGURE 1. Block diagram of the TX, where M $\pi/2$-BPSK symbols with extra constellation rotation are transmitted using $L \geq M$ sub-carriers.

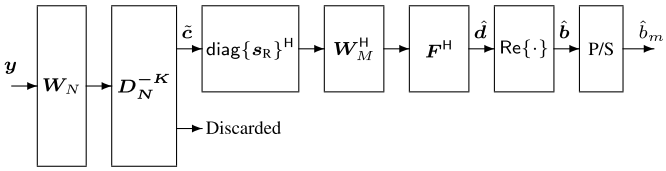

FIGURE 2. Block diagram of RX, where a length-N vector $\boldsymbol{y}$ is processed to estimate the M BPSK symbols in $\boldsymbol{b}$.

which conforms to how the standards converts BPSK symbols to $\pi/2$-BPSK symbols [13], [14].

In the third block, the $\pi/2$-BPSK symbol vector $\boldsymbol{Fb}$ is pre-multiplied by the extra constellation-rotation matrix defined as

$$\boldsymbol{R}(\phi) \triangleq \mathrm{diag}\left\{\left[e^{\mathrm{j}\phi\cdot 0}, e^{\mathrm{j}\phi\cdot 1}, \ldots, e^{\mathrm{j}\phi\cdot(M-1)}\right]\right\} \tag{2}$$

with rotation angle ϕ. The standards have $\phi = 0$, which leads to $\boldsymbol{R}(0) = \boldsymbol{I}_M$ with $\boldsymbol{I}_M$ being the identity matrix of size M.

In the fourth and fifth blocks, the generalized FDSS is performed. In the fourth block, the M-point DFT-spreading and circular extension are performed. Then, the one-tap spectrum shaping is performed in the fifth block. Let $\boldsymbol{W}_{L,M}$ be the extended DFT matrix obtained by circularly extending the rows of the unitary M-by-M DFT matrix $\boldsymbol{W}_M$. That is, the (i,j)th entry of the L-by-M matrix $\boldsymbol{W}_{L,M}$ is given by

$$\left[\boldsymbol{W}_{L,M}\right]_{(i,j)} \triangleq \frac{1}{\sqrt{M}} e^{-\mathrm{j}\frac{2\pi}{M}(i-1)(j-1)} \tag{3}$$

for $1 \leq i \leq L$ and $1 \leq j \leq M$. When $L = M$, $\boldsymbol{W}_{L,M}$ becomes $\boldsymbol{W}_M$. Hence, the output of the fifth block can be rewritten as

$$\boldsymbol{c} \triangleq \mathrm{diag}\{\boldsymbol{s}_T\}\boldsymbol{W}_{L,M}\boldsymbol{R}(\phi)\boldsymbol{Fb}, \tag{4}$$

where $\boldsymbol{s}_T$ is an L-by-1 FDSS vector or, simply, shaping vector given by

$$\boldsymbol{s}_T \triangleq \left[s_{T,1}, s_{T,2}, \ldots, s_{T,L}\right]^T \tag{5}$$

with ^{T} denoting transposition. We assume that L is also an even number throughout this paper as M is. By setting $s_{T,1} = 0$, we can simply accommodate a shaping vector of effective length $L-1$, an odd number.

In the sixth block, the FD signal vector $\boldsymbol{c}$ is first augmented by the all-zero vector $\boldsymbol{0}_{N-L}$ of length-$(N-L)$ and then circular downshifted by K_T as

$$\boldsymbol{a} \triangleq \boldsymbol{D}_N^{K_T}\begin{bmatrix}\boldsymbol{c}\\ \boldsymbol{0}_{N-L}\end{bmatrix}, \tag{6a}$$

where $\boldsymbol{D}_N$ is given as

$$[\boldsymbol{D}_N]_{(i,j)} \triangleq \begin{cases} 1, & \text{for } i = \mathrm{mod}(j,N)+1 \\ 0, & \text{elsewhere,}\end{cases} \tag{6b}$$

for $1 \leq i,j \leq N$, with $\mathrm{mod}(\cdot,N)$ denoting the modulo-N operation, and the exponent K_T is given by

$$K_T \triangleq K - \frac{L-M}{2}. \tag{6c}$$

This choice of K_T makes the length-L FD signal vector $\boldsymbol{c}$ be allocated to the frequency band ranging from the (K_T+1)th to (K_T+L)th sub-carriers, which includes the assigned $(K+1)$th to $(K+M)$th sub-carriers in its center. It also makes $K_T = K$ if $L = M$.

In the seventh block, the N-point inverse DFT (IDFT) is performed to generate an OFDM symbol vector $\boldsymbol{x}$, i.e.,

$$\boldsymbol{x} \triangleq \boldsymbol{W}_N^H\boldsymbol{a}, \tag{7}$$

where the superscript ^{H} denotes Hermitian transposition.

In Fig. 1, a block to add a length-N_{CP} cyclic prefix (CP) to the OFDM symbol vector $\boldsymbol{x}$, a parallel-to-serial converter (P/S) block, and a digital-to-analog converter (D/A) block are omitted. The P/S block converts the sequence of CP-added OFDM symbol vectors to a discrete-time (DT) signal. The D/A block converts the DT signal to a continuous-time (CT) signal $x(t)$, which is the complex envelope of a real-valued bandpass signal that will pass through a nonlinear PA.

Note that, if $\phi = 0$ and $L = M$, this TX for a generalized FDSS reduces to that for the ordinary FDSS in the standards. After the RX structure that conforms to the standards is described in the following subsection, we present in the next section the proposed shaping vector $\boldsymbol{s}_T^*$ of length $L > M$ and extra rotation angle ϕ^* that is not zero in general.[1] It will be shown that the proposed design makes the PA input be an almost CE signal, that the PA output has negligible OOB emission compared to the conventional design, and that the RX output achieves an outstanding EVM performance.

B. RECEIVER

It is assumed that the complex envelope of the received signal is modeled by $y(t) = h(t) * x(t) + z(t)$, where $h(t)$ is the channel impulse response whose delay spread is less than N_{cp} samples and $z(t)$ is a complex additive white Gaussian noise (AWGN).

We consider the reception of the first BPSK symbol vector. Fig. 2 shows the block diagram of the RX in complex baseband, which is a conventional one-tap FDE followed by the real-part operator to generate the estimate $\hat{\boldsymbol{b}}$ of $\boldsymbol{b}$. An analog-to-digital converter (A/D) block, an S/P block that converts the CT signal $y(t)$ to a sequence of length $(N+N_{cp})$ vectors, and a CP removal block are omitted. Then, the length-N vector $\boldsymbol{y}$ is obtained as

$$\boldsymbol{y} = \boldsymbol{Hx} + \boldsymbol{z}, \tag{8}$$

1. In this paper, $*$ as a superscript denotes a proposed design parameter. As an operator, it denotes convolution.

where $\boldsymbol{H}$ is an N-by-N circulant channel matrix and $\boldsymbol{z}$ is a complex Gaussian random vector of length N, i.e., $\boldsymbol{z} \sim \mathcal{CN}(\boldsymbol{0}_N, \sigma^2 \boldsymbol{I}_N)$ for some $\sigma^2 > 0$.

The first and second blocks, respectively, pre-multiply the DFT matrix $\boldsymbol{W}_N$ to $\boldsymbol{y}$ and select the assigned M sub-carriers from the DFT output. Notice that the amount K of circular upshifting in the second block is different from K_{T} used in the TX if $L > M$. Let $\boldsymbol{T}_{M,N}$ be the truncation matrix that keeps only the first M rows and discards the rest $N - M$ rows, i.e.,

$$\boldsymbol{T}_{M,N} \triangleq \left[\boldsymbol{I}_M \; \boldsymbol{O}_{M\times(N-M)}\right], \tag{9a}$$

where $\boldsymbol{O}_{M\times(N-M)}$ is the M-by-$(N-M)$ all zero matrix. Then, the length-M vector $\tilde{\boldsymbol{c}}$ at the output of the second block is given by

$$\tilde{\boldsymbol{c}} = \boldsymbol{T}_{M,N}\boldsymbol{D}_N^{-K}\boldsymbol{W}_N\boldsymbol{y}. \tag{9b}$$

The third block performs the one-tap equalization by pre-multiplying $\mathsf{diag}\{\boldsymbol{s}_{\mathrm{R}}\}^{\mathsf{H}}$ to $\tilde{\boldsymbol{c}}$, and then the fourth and fifth blocks reverse the DFT-spreading and phase-shifting operations at the TX to form

$$\hat{\boldsymbol{d}} = \boldsymbol{F}^{\mathsf{H}}\boldsymbol{W}_M^{\mathsf{H}}\mathsf{diag}\{\boldsymbol{s}_{\mathrm{R}}\}^{\mathsf{H}}\tilde{\boldsymbol{c}}. \tag{10}$$

The sixth block generates $\hat{\boldsymbol{b}} = \mathsf{Re}\{\hat{\boldsymbol{d}}\}$ by taking the real part of $\hat{\boldsymbol{d}}$, and the last P/S block generates the estimate $\hat{b}_m$ of b_m.

Notice that the circular shift, one-tap equalization, and IDFT are performed as if the TX has $L = M$ by multiplying $\boldsymbol{D}_N^{-K}$, $\mathsf{diag}\{\boldsymbol{s}_{\mathrm{R}}\}^{\mathsf{H}}$, and $\boldsymbol{W}_M^{\mathsf{H}}$, respectively. Hence, the RX is fully compatible with the current standards.

III. PROPOSED DESIGN AND ITS PROPERTIES

In this section, we propose the combinations of a shaping vector and an extra constellation rotation angle that can generate almost CE signals at the TX. Then, the proposed design is shown to satisfy one desirable condition and one necessary condition. It is compared with conventional designs in terms of these two conditions.

A. PROPOSED S_T AND ϕ

Motivated by the fact that the conventional single-carrier MSK achieves 0 dB PAPR by generating a perfect CE signal, we define the MSK transmit pulse $p(t)$ as the time-limited cosine function $\cos(\pi t/2)$ truncated to $t \in [-1, 1]$. It is well known that its CT Fourier transform (CTFT) is real and symmetrical about $f = 0$ and given by

$$P(f) = \mathrm{sinc}\left(-2f + \frac{1}{2}\right) + \mathrm{sinc}\left(2f + \frac{1}{2}\right), \tag{11}$$

where $\mathrm{sinc}(x) = 1$ for $x = 0$ and $\sin(\pi x)/\pi x$ elsewhere.

The proposed shaping vector $\boldsymbol{s}_{\mathrm{T}}^*$ has the lth element given by

$$s_{\mathrm{T},l}^* \triangleq \mathrm{sinc}\left(\frac{-2l + L^* + 2}{M} + \frac{1}{2}\right) + \mathrm{sinc}\left(\frac{2l - L^* - 2}{M} + \frac{1}{2}\right), \tag{12a}$$

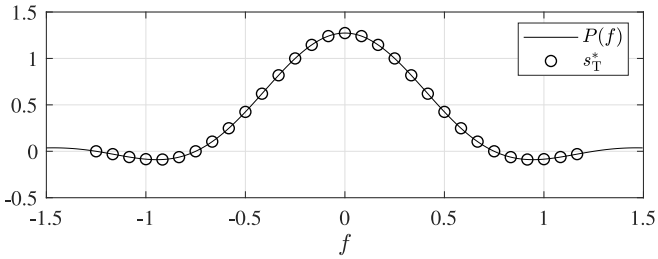

FIGURE 3. Proposed shaping vector when $M = 12$ and $L = 30$.

for $l = 1, 2, \ldots, L^*$, where

$$L^* = \frac{M}{2} + kM \tag{12b}$$

for $k = 1, 2, \ldots,$. Fig. 3 shows an example of the proposed shaping vector when $M = 12$ and $L = L^* = 30$ with $k = 2$.

Notice that $\boldsymbol{s}_{\mathrm{T}}^*$ is obtained by uniformly sampling $P(f)$ at the rate of M samples per unit frequency. Since the absolute bandwidth of $p(t)$ is infinity, only L^* samples are taken from $P(f)$. Recall that $P(f)$ in (11) crosses zero at $|f| = 3/4 + k/2$ for $k = 1, 2, \ldots$ Hence, this choice of L in (12b) reduces the effective length of $\boldsymbol{s}_{\mathrm{T}}^*$ to $L^* - 1$, an odd number, because $s_{\mathrm{T},1}^* = 0$. Now, the rest $L^* - 1$ elements are real and symmetrical about $l = L^*/2 + 1$ with $s_{\mathrm{T},L^*/2+1}^* = P(0)$.

The proposed extra rotation angle is given by

$$\phi^* \triangleq \mathsf{mod}\left(\frac{L^* - M}{M}\pi, 2\pi\right). \tag{13}$$

Since $\mathsf{mod}((L-M)\pi/M, 2\pi) = 0$ if and only if L is an odd multiple of M, the proposed L^* in (12b) makes the proposed extra rotation angle ϕ^* never equal to 0.

Figs. 4-(a) and (b) show, in the first and second rows, the trajectories and the envelopes of the complex envelope $x(t)$ of the PA input when we choose $M = 12$ consecutive sub-carriers and choose $L^* = 18$ and 30, respectively. For convenience, the signal power is normalized. The OFDM symbol vector $\boldsymbol{x}$ of length N and two neighboring OFDM symbol vectors, each with length-N_{cp} CPs, are generated and fed to the D/A block to obtain $x(t)$, where $N = 1024$ and $N_{\mathrm{cp}} = 72$. Each trajectory figure shows 64 randomly generated $x(t)$ superimposed in the complex plane and each envelope figure shows a typical sample path of $|x(t)|$ both for $-0.5T \le t \le 1.5T$, where the OFDM symbol of interest resides in the middle of the time period from 0 to T.

Apparently, the trajectory figures in the first row show that $x(t)$ is far from a perfect CE signal. However, the real and imaginary parts and the envelopes in the second to fourth rows reveal that the abrupt changes in the magnitude and phase of $x(t)$ are located only at the boundaries between two OFDM symbols, where discontinuity inherent to any OFDM-based block transmission occurs. Fortunately, as well pointed out in [21], the bandwidth of an uplink transmit filter is often much larger than the bandwidth of the transmitted signal. This is because the number and location of the assigned consecutive sub-carriers can vary in

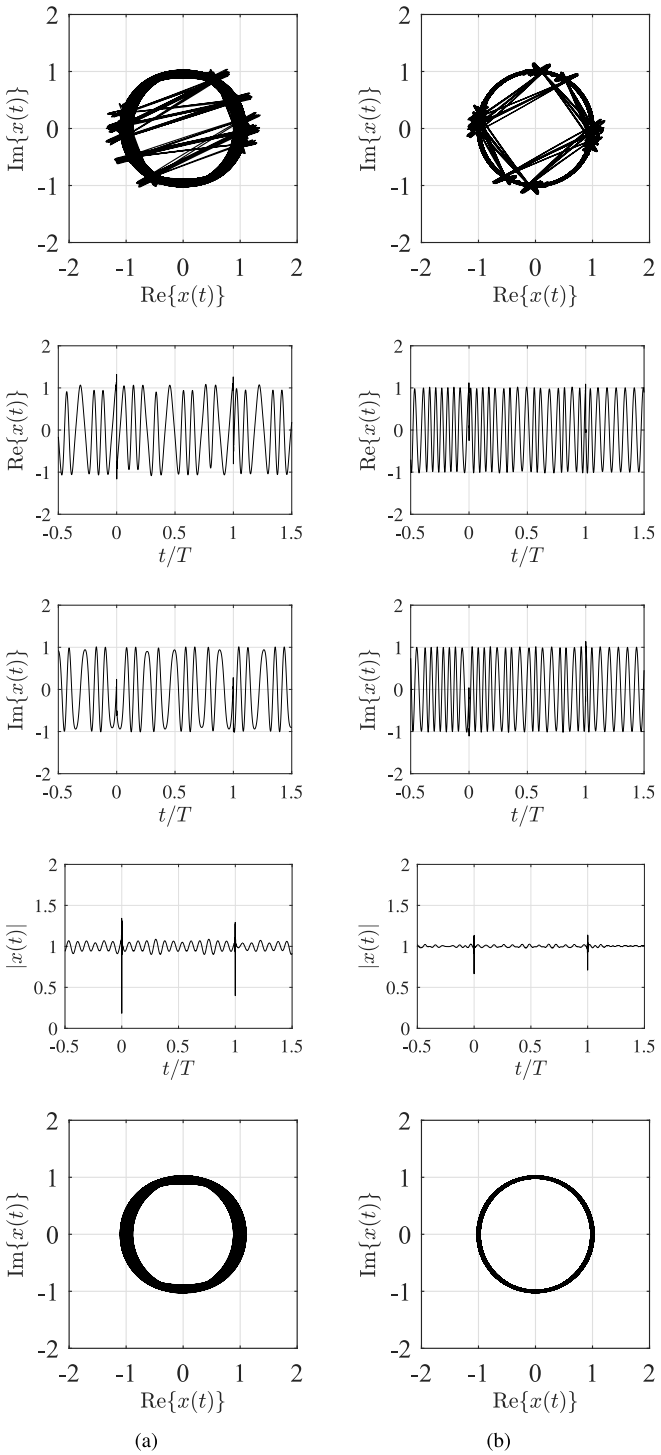

FIGURE 4. Trajectories, real and imaginary parts, and envelopes of x(t) when the proposed $\mathbf{s}_{\mathrm{T}}^{*}$ and ϕ^{*} are used for $M = 12$ and $N = 1024$. The fifth row shows the trajectories when the boundaries between two OFDM symbols are symbols: (a) $L^{*} = 18$ and (b) $L^{*} = 30$.

the DFT-spread OFDM. Similar to the Gibbs phenomenon with a filter of large bandwidth, if $M \ll N$, which is the case with IoT devices, then such a magnitude and phase deviation is limited to small time durations around the integer multiples of T and, consequently, the error signal has very small energy. In the fifth row of Fig. 4, the trajectories of $x(t)$ are shown when time intervals corresponding to the boundaries between two OFDM symbols are removed. It can be seen that an almost CE signal can be obtained by using $L^{*} = 30$. Moreover, the nonlinear PA operating with a small OBO to achieve a high power efficiency suppresses the overshoot of the envelope, which reduces the signal distortion. Hence, as it will be shown in Section IV, the effective signal-to-distortion ratio (SDR) [15] measured at the PA output for the first BPSK symbol is several tens of dB for various combinations of L, M, and $N \gg M$. Although not of our interest in this paper, if $M \ll N$, then a technique similar to the trellis termination used in [7] can be applied to keep the magnitude and phase continuity at the boundaries.

B. I/Q ORTHOGONALITY AND COMPATIBILITY CONDITIONS

In this subsection, we introduce the inphase-quadrature (I/Q) orthogonality condition and compatibility condition. We show that the proposed design satisfies both of the conditions. To proceed, we define symbol waveforms and the I/Q orthogonality.

Definition: The N-by-M matrix $\boldsymbol{G}$ defined as

$$\boldsymbol{G} \triangleq \boldsymbol{W}_N^{\mathsf{H}} \boldsymbol{D}_N^{K_{\mathrm{T}}} \begin{bmatrix} \mathrm{diag}\{\boldsymbol{s}_{\mathrm{T}}\} \boldsymbol{W}_{L,M} \boldsymbol{R}(\phi) \\ \boldsymbol{O}_{(N-L)\times M} \end{bmatrix} \tag{14}$$

is called the symbol waveform matrix for the $\pi/2$-BPSK symbol vector $\boldsymbol{Fb}$. The mth column $\boldsymbol{g}_m$ of $\boldsymbol{G}$ is called the symbol waveform vector for the mth $\pi/2$-BPSK symbol, because

$$\boldsymbol{x} = \boldsymbol{GFb} = \boldsymbol{g}_1 b_1 + \mathrm{j}\boldsymbol{g}_2 b_2 + \cdots + \mathrm{j}\boldsymbol{g}_M b_M \tag{15}$$

by (7) and (14) and by the assumption that M is even.

Definition: Let $g_m[n]$ be the nth element of $\boldsymbol{g}_m$. Then, the I/Q components of the generated signal are called orthogonal if the relative phase angle between two entries in the same row of $\boldsymbol{G}$ satisfies

$$\mathrm{mod}\left(\angle \frac{g_m[n]}{g_{m'}[n]}, 2\pi \right) = 0 \text{ or } \pi \tag{16}$$

for all $m, m' = 1, 2, \ldots, M$, and $n = 1, 2, \ldots, N$, such that $g_m[n] g_{m'}[n] \neq 0$.

This definition is motivated by the fact that transmitted signals of the conventional single-carrier OQPSK, MSK, and OQAM with real symmetrical transmit pulses all have perfect phase orthogonality between two consecutive real-valued symbols. This condition is desirable because otherwise the PAPR increases at the TX given the same transmit pulse, and intersymbol interference may occur at the RX. As seen in (15), the condition (16) makes the relative phase angle between two consecutive entries in the same row of $\boldsymbol{GF}$ equal to $\pm\pi/2$.

Proposition: Given any $\boldsymbol{s}_{\mathrm{T}}$ that has an odd effective length $L-1$ and is real symmetric, i.e.,

$$s_{\mathrm{T},l} = 0, \text{ for } l = 1, \text{ and} \tag{17a}$$

$$s_{\mathrm{T},l} = s_{\mathrm{T},L-l+2}, \text{ for } l = 2, 3, \ldots, L, \tag{17b}$$

the I/Q orthogonality condition (16) is satisfied if and only if

$$\phi = \frac{L}{M}\pi + k\pi \tag{18}$$

for some integer k.

Proof: By the assumptions on the shaping vector $\boldsymbol{s}_{\mathrm{T}}$, $g_m[n]$ can be simplified as

$$g_m[n] = \frac{e^{\mathrm{j}\frac{2\pi}{N}(n-1)K_{\mathrm{T}}}e^{\mathrm{j}\phi(m-1)}}{\sqrt{MN}} \sum_{l=1}^{L} s_{\mathrm{T},l} e^{\mathrm{j}2\pi(l-1)\psi_m[n]} \tag{19a}$$

$$= \frac{e^{\mathrm{j}\frac{2\pi}{N}(n-1)K_{\mathrm{T}}}e^{\mathrm{j}\phi(m-1)}}{\sqrt{MN}} \times \left[s_{\mathrm{T},\frac{L}{2}+1} e^{\mathrm{j}\pi L\psi_m[n]} + \sum_{l=2}^{L/2} s_{\mathrm{T},l}\left\{ e^{\mathrm{j}2\pi(l-1)\psi_m[n]} + e^{\mathrm{j}2\pi(L-l+1)\psi_m[n]} \right\} \right] \tag{19b}$$

$$= \frac{f_m[n]}{\sqrt{MN}} e^{\mathrm{j}\frac{\pi}{N}(2K_{\mathrm{T}}+L)(n-1)} e^{\mathrm{j}\left(\phi-\frac{L}{M}\pi\right)(m-1)}, \tag{19c}$$

where $\psi_m[n] \triangleq (n-1)/N - (m-1)/M$ and

$$f_m[n] \triangleq s_{\mathrm{T},\frac{L}{2}+1} + 2\sum_{l=2}^{L/2} s_{\mathrm{T},l} \mathrm{Re}\left\{ e^{\mathrm{j}\pi(L-2l+2)\psi_m[n]} \right\}. \tag{20}$$

Note that $f_m[n]$ is real for all m and n, and that $g_m[n]/f_m[n]$ can be factored into two functions only of m and n, respectively. Hence, the relative phase angle is given by

$$\angle \frac{g_m[n]}{g_{m'}[n]} = \left(\phi - \frac{L}{M}\pi\right)(m-m') + \angle \frac{f_m[n]}{f_{m'}[n]} \tag{21a}$$

$$= \left(\phi - \frac{L}{M}\pi\right)(m-m') + k\pi \tag{21b}$$

for some integer k. Therefore, the conclusion follows. ■

It can be seen that the proposed ϕ^* together with the proposed $\boldsymbol{s}_{\mathrm{T}}^*$ satisfies this I/Q orthogonality condition. For the compatibility, we need the following definition.

Definition: Similarly to $\boldsymbol{T}_{M,N}$ in (9a), let $\boldsymbol{T}_{M,L}$ be the M-by-L truncation matrix. Then, the RX is compatible with the current standards in [13], [14] if

$$\boldsymbol{T}_{M,L}\boldsymbol{D}_L^{K_{\mathrm{T}}-K}\boldsymbol{W}_{L,M}\boldsymbol{R}(\phi) = \boldsymbol{W}_M. \tag{22}$$

This definition is motivated by the fact that the observed signal $\tilde{\boldsymbol{c}}$ in (9b) can be rewritten as

$$\tilde{\boldsymbol{c}} = \boldsymbol{T}_{M,N}\boldsymbol{D}_N^{-K}\boldsymbol{W}_N(\boldsymbol{H}\boldsymbol{x} + \boldsymbol{z}) \tag{23a}$$

$$= \tilde{\boldsymbol{H}}\mathrm{diag}\{\tilde{\boldsymbol{s}}_{\mathrm{T}}\}\boldsymbol{T}_{M,L}\boldsymbol{D}_L^{K_{\mathrm{T}}-K}\boldsymbol{W}_{L,M}\boldsymbol{R}(\phi)\boldsymbol{F}\boldsymbol{b} + \tilde{\boldsymbol{z}} \tag{23b}$$

where $\tilde{\boldsymbol{H}}$ is an M-by-M diagonal channel matrix, $\tilde{\boldsymbol{s}}_{\mathrm{T}}$ is a length-M row-pruned shaping vector and $\tilde{\boldsymbol{z}}$ is a length-M AWGN vector defined as $\tilde{\boldsymbol{H}} \triangleq \boldsymbol{T}_{M,N}\boldsymbol{D}_N^{-K}\boldsymbol{W}_N\boldsymbol{H}\boldsymbol{W}_N^{\mathsf{H}}\boldsymbol{D}_N^{K}\boldsymbol{T}_{M,N}^{\mathsf{H}}$, $\tilde{\boldsymbol{s}}_{\mathrm{T}} \triangleq \boldsymbol{T}_{M,L}\boldsymbol{D}_L^{K_{\mathrm{T}}-K}\boldsymbol{s}_{\mathrm{T}}$, and $\tilde{\boldsymbol{z}} \triangleq \boldsymbol{T}_{M,N}\boldsymbol{D}_N^{-K}\boldsymbol{W}_N\boldsymbol{z}$, respectively. Then, the condition (22) makes $\tilde{\boldsymbol{c}}$ not a function of ϕ as

$$\tilde{\boldsymbol{c}} = \tilde{\boldsymbol{H}}\mathrm{diag}\{\tilde{\boldsymbol{s}}_{\mathrm{T}}\}\boldsymbol{W}_M\boldsymbol{F}\boldsymbol{b} + \tilde{\boldsymbol{z}}, \tag{24}$$

where the extra constellation rotation by ϕ performed at the TX has no effect. Hence, the one-tap FDE described in Section II-B has the observation $\tilde{\boldsymbol{c}}$ as if the extra rotation angle is zero.

Proposition: Given any shaping vector $\boldsymbol{s}_{\mathrm{T}}$ of length L, an even number, the compatibility condition (22) is satisfied if and only if

$$\phi = \frac{L-M}{M}\pi + 2k\pi \tag{25}$$

for some integer k.

Proof: The (i,j)th elements of $\boldsymbol{T}_{M,L}\boldsymbol{D}_L^{K_{\mathrm{T}}-K}\boldsymbol{W}_{L,M}\boldsymbol{R}(\phi)$ and $\boldsymbol{W}_M$ can be written, respectively, as

$$\left[\boldsymbol{T}_{M,L}\boldsymbol{D}_L^{K_{\mathrm{T}}-K}\boldsymbol{W}_{L,M}\boldsymbol{R}(\phi)\right]_{(i,j)} = \frac{1}{\sqrt{M}} e^{-\mathrm{j}\frac{2\pi}{M}(i-1-K_{\mathrm{T}}+K)(j-1)} e^{\mathrm{j}\phi(j-1)} \tag{26a}$$

$$= \frac{1}{\sqrt{M}} e^{-\mathrm{j}\frac{2\pi}{M}\left(i-1-K_{\mathrm{T}}+K-\frac{M\phi}{2\pi}\right)(j-1)} \tag{26b}$$

and $e^{-\mathrm{j}\frac{2\pi}{M}(i-1)(j-1)}/\sqrt{M}$, for $1 \le i,j \le M$. Hence, the condition (22) is met if and only if

$$K_{\mathrm{T}} - K + \frac{M\phi}{2\pi} = Mk \tag{27}$$

for some integer k. Therefore, the conclusion follows by the definition of K_{T} in (6c). ■

It can be seen that the proposed ϕ^* satisfies this compatibility condition. Now, we show that the proposed ϕ^* is the unique extra rotation angle satisfying both the I/Q orthogonality and compatibility conditions when $\boldsymbol{s}_{\mathrm{T}}$ is real and symmetrical.

Theorem: (i) Given any $\boldsymbol{s}_{\mathrm{T}}$ that is a real symmetric vector of an odd effective length as (17a), the proposed ϕ^* is the unique extra rotation angle that satisfies both the I/Q orthogonality and compatibility conditions at the same time. (ii) Given any $\boldsymbol{s}_{\mathrm{T}}$ that is real symmetric vector of an even effective length as $s_{\mathrm{T},l} = s_{\mathrm{T},L-l+1}$, for $l = 1, 2, \ldots, L$, there is no extra rotation angle that simultaneously satisfies the I/Q orthogonality and compatibility conditions.

Proof: (i) By Propositions 1 and 2, the conclusion follows immediately. (ii) As shown in Lemma 1 [10], the relative phase angle between two consecutive entries in the same row of $\boldsymbol{GF}$ is equal to $\pm\pi/2$ if and only if $\phi = (L-1)\pi/M + k\pi$ for some integer k. However, this ϕ always violates the compatibility condition (25). Therefore, the conclusion follows. ■

This theorem justifies why the proposed $\boldsymbol{s}_{\mathrm{T}}^*$ and ϕ^* are chosen as (12a) and (13), respectively. It also explains why the generalized FDSS technique proposed in [10], which has $\phi = (L-1)\pi/M + k\pi$ in effect, is not compatible with the current standards.

Since the CTFT $P(f)$ of the MSK transmit pulse, which generates a perfect CE signal, is a real symmetric function about $f = 0$ as seen in (11), the only way to use a uniformly

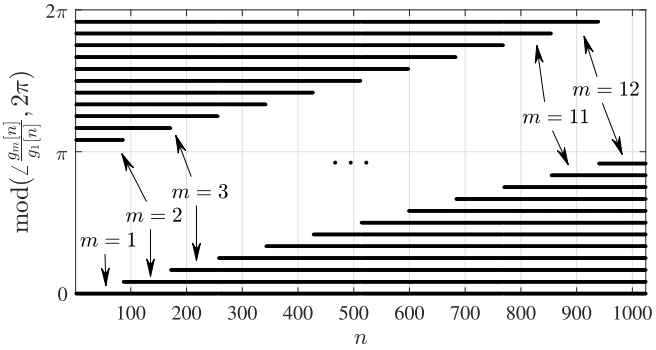

FIGURE 5. Relative phase angle as a function of n when DFT-spread OFDM without FDSS is considered.

sampled $P(f)$ as the shaping vector is to sample as (12a) and to have L^* as (12b). Hence, the proposed design with the shaping vector $\boldsymbol{s}_{\mathrm{T}}^*$ of an odd effective length as (17a) and the extra rotation angle ϕ^* satisfies the I/Q orthogonality condition and, consequently, makes the input signal to a nonlinear PA similar to the MSK signal. Of course, even if L^* does not satisfy (12b), any choice of $L^* \gg M$ with $\phi^* = \mathsf{mod}((L^* - M)\pi/M, 2\pi)$ can make the orthogonality condition approximately satisfied because $\lim_{f\to-\infty} P(f) = 0$ implies $s_{\mathrm{T},1}^* \approx 0$. For example, if $L^* \gg M$ is an odd multiple of M and $\phi^* = 0$, or if $L^* \gg M$ is an even multiple of M and $\phi^* = \pi$, then the orthogonality condition is approximately satisfied. Hence, the restriction on L^* in (12b) can be relaxed.

C. COMPARISON TO CONVENTIONAL DESIGNS

In this subsection, the proposed design is compared with conventional ones. First, we consider the DFT-spread OFDM without FDSS, which has $L = M$, $\phi = 0$, and $\boldsymbol{s}_{\mathrm{T}} = \mathbf{1}_M$, where $\mathbf{1}_M$ is the length-M vector of all ones. Since $\mathbf{1}_M$ is even symmetric, but M is a multiple of 12 in the standards, this design violates the I/Q orthogonality condition. Fig. 5 shows the relative phase angle $\mathsf{mod}(\angle g_m[n]/g_1[n], 2\pi)$ as a function of n for $m = 1, 2, \ldots, M$ when $L = M = 12, N = 1024$, $\phi = 0$, and $\boldsymbol{s}_{\mathrm{T}} = \mathbf{1}_{12}$. Notice that the relative phase angles between two consecutive entries in the same row of $\boldsymbol{GF}$ are not equal to $\pm\pi/2$ but have the additional phase angles of $\pm\pi/M$, so that the I/Q orthogonality condition is violated.

Second, we consider the FDSS employing the 3-tap TD filter in [9]. The TD implementation multiplies a circulant matrix having the first row $[1, -0.28, \mathbf{0}_{M-3}^{\mathsf{T}}, -0.28]$ to the $\pi/2$-BPSK symbol vector $\boldsymbol{Fb}$ and then multiplies the DFT matrix of size M to obtain $\boldsymbol{c}$ in (4). This is equivalent to having $L = M$, $\phi = 0$, and $\boldsymbol{s}_{\mathrm{T}}$ given by

$$\boldsymbol{s}_{0.28} = \boldsymbol{W}_M \begin{bmatrix} 1 \\ -0.28 \\ \mathbf{0}_{M-3} \\ -0.28 \end{bmatrix}. \tag{28}$$

It turns out that $s_{0.28,l} = s_{0.28,L-l+2}$, for $l = 2, 3, \ldots, L$, but $s_{0.28,1}$ has a small non-zero value. Hence, the compatibility condition is satisfied but the I/Q orthogonality condition is approximately satisfied. As it will be seen in the next section, however, the PAPR and EVM performance of this filter is not as good as the proposed design because no excess sub-carrier is utilized to better shape the symbol waveform vectors.

Third, we consider the TD filters proposed in [8]. All the designs have $L = M$ and $\phi = 0$, but the circulant matrix for TD filtering has different first rows. For example, the equivalent shaping vector of the type A-2 filter is given by

$$\boldsymbol{s}_{\text{A-2}} = \boldsymbol{D}_M^{\frac{L}{2}} \boldsymbol{W}_M \begin{bmatrix} 0.9285 \\ 0.2609 \\ 0.0007 \\ \mathbf{0}_{M-5} \\ 0.0007 \\ 0.2609 \end{bmatrix}. \tag{29}$$

The equivalent shaping vectors of the other TD filters can be derived in the same way as (29). It turns out that, similar to (28), the equivalent shaping vectors of the type A filters are real symmetric about $l = L/2 + 1$ but have small non-zero first elements. Hence, the compatibility condition is satisfied but the I/Q orthogonality condition is approximately satisfied. The equivalent shaping vectors of the type B filters are conjugate symmetrical about $l = L/2 + 1$ and have zero first elements. As shown in the following corollary, this makes the type B filters satisfy both the I/Q orthogonality and compatibility conditions.

Corollary: (i) Given any $\boldsymbol{s}_{\mathrm{T}}$ that is a conjugate symmetric vector of an odd effective length as $s_{\mathrm{T},1} = 0$ and $s_{\mathrm{T},l} = \bar{s}_{\mathrm{T},L-l+2}$, for $l = 2, 3, \ldots, L$, where $\bar{}$ denotes complex conjugation, the proposed ϕ^* is the unique extra rotation angle that satisfies both the I/Q orthogonality and compatibility conditions at the same time. (ii) Given any $\boldsymbol{s}_{\mathrm{T}}$ that is conjugate symmetric vector of an even effective length as $s_{\mathrm{T},l} = \bar{s}_{\mathrm{T},L-l+1}$, for $l = 1, 2, \ldots, L$, there is no extra rotation angle that simultaneously satisfies the I/Q orthogonality and compatibility conditions.

Proof: (i) It can be shown that the conjugate symmetry condition still leads to (21a) in Propositions 1 if $f_m[n]$ in (20) is modified as

$$f_m[n] \triangleq s_{\mathrm{T},\frac{L}{2}+1} + 2\sum_{l=2}^{L/2} \mathrm{Re}\left\{\bar{s}_{\mathrm{T},l} e^{\mathrm{j}\pi(L-2l+2)\psi_m[n]}\right\}. \tag{30}$$

Moreover, the compatibility condition is not affected by the conjugate symmetry of $\boldsymbol{s}_{\mathrm{T}}$. Therefore, the conclusion follows. (ii) It can be shown that a similar modification to (30) makes Lemma 1 in [10] still hold with $\phi = (L-1)\pi/M + k\pi$ for some integer k. Therefore, the conclusion follows because the relative phase angle $\angle(g_m[n]/g_{m'}[n])$ becomes an integer multiple of π. ■

However, as shown in the next section, these filters are not as good as the proposed design, because no excess sub-carrier is utilized. Of course, the TD implementation of the FDSS such as [8] and [9] may have less computational complexity

than the FD implementation if the number of taps is small. Unfortunately, to our best knowledge, no extension of the TD implementation is available yet to the systems with excess sub-carriers, i.e., $L > M$.

Finally, we consider the FDSS employing square-root raised cosine (SRRC) shaping vectors. In [22], SRRC shaping vectors of odd effective lengths are proposed for the DFT-spread OFDM of QPSK symbols to utilize excess sub-carriers in shaping the symbol waveform vectors, where the SRRC shaping vector $\boldsymbol{s}_{\text{SRRC}}$ with $M < L \le 2M$ is given by

$$s_{\text{SRRC},l} \triangleq \begin{cases} \sin\left(\frac{\pi(l-1)}{2(L-M)}\right), & \text{for } 1 \le l \le L-M, \\ \cos\left(\frac{\pi(l-M-1)}{2(L-M)}\right), & \text{for } M+1 \le l \le L, \\ 1, & \text{elsewhere.} \end{cases} \quad (31)$$

It can satisfy both the I/Q orthogonality and compatibility conditions when $\phi = (L-M)\pi/M$ and $K_{\text{T}} = K-(L-M)/2$, because $s_{\text{SRRC},1} = 0$ and $s_{\text{SRRC},l} = s_{\text{SRRC},L-l+2}$, for $l = 2, 3, \ldots, L$. The factor $(L-M)$ appearing in (31) is related to the roll-off factor β as

$$\beta = \frac{L-M}{M} \quad (32)$$

of the SRRC shaping vector. This roll-off factor can be regarded as the excess bandwidth [23, Sec. 11.3] of the shaping vector. As shown in (31), the SRRC shaping vectors have an advantage in that they can be easily obtained from a closed-form formula for various combinations of M and $M < L \le 2M$. However, as it will be seen in the next section, this design results in large OOB emission and poor PAPR and EVM performances.

IV. NUMERICAL RESULTS

In this section, numerical results are provided that compare the proposed and conventional designs described in the previous section. To proceed, we briefly discuss the performance metrics used in the comparison.

A. PERFORMANCE METRICS

The first metric is the PAPR measured at the input of the nonlinear PA. The PAPR of the complex envelope $x(t)$ of a real-valued bandpass signal is defined as

$$\text{PAPR} \triangleq \max_{0 \le t \le T} \frac{|x(t)|^2}{\text{E}\{|x(t)|^2\}}. \quad (33)$$

As illustrated in Fig. 4, this definition in terms of a CT signal may overestimate the PAPR. This is because, under the assumption of $M \ll N$, an abrupt change in the magnitude and phase of $x(t)$ around the integer multiples of T increases the numerator of (33) a lot but has little effect on the denominator of (33). Hence, we consider a sampled-signal PAPR given by

$$\text{PAPR}^* \triangleq \frac{\|\boldsymbol{x}\|_\infty^2}{\text{E}\{\|\boldsymbol{x}\|^2\}}, \quad (34)$$

where $\boldsymbol{x}$ is a length-N vector defined in (7), the infinity norm $\|\cdot\|_\infty$ denotes the maximum absolute value of the elements, and $\|\cdot\|$ denotes the 2-norm of a vector. It is nothing but the PAPR of the DT signal obtained by sampling the CT signal $x(t)$ N times per OFDM symbol, and well reflects the envelope fluctuation of the signal except around the integer multiples of T.

This metric is easy to compute exactly or approximately and has been commonly used in [10], [24]–[28] to analyze the PAPR of DFT-spread I-OFDM and L-OFDM signals. As shown soon in the next subsection, although measured at the input of a PA, the sampled-signal PAPR in (34) is a good predictor of the robustness of an input signal to the nonlinearity of the PA.

The second metric is the effective SDR or, equivalently, the EVM measured at the output of the nonlinear PA. The effective SDR is defined as

$$\text{SDR}_{\text{eff}} \triangleq \frac{M}{\text{E}\left\{\left\|\boldsymbol{b} - \text{Re}\left\{\lambda_{\text{opt}}\hat{\boldsymbol{d}}\right\}\right\|^2\right\}}, \quad (35)$$

where the complex number λ_{opt} is given by $\lambda_{\text{opt}} \triangleq \arg\min_\lambda \text{E}\{\|\boldsymbol{b} - \text{Re}\{\lambda\hat{\boldsymbol{d}}\}\|^2\}$. In terms of the effective SDR, the EVM in percentage is defined as [15], [29]–[31]

$$\text{EVM}(\%) \triangleq \frac{1}{\sqrt{\text{SDR}_{\text{eff}}}} \times 100. \quad (36)$$

The EVM or, equivalently, the effective SDR can be computed under different assumptions on system imperfections, channels, and the RX structure. As in [15], we consider the performance of a RX that assumes an ideal amplifier and operates in a frequency-flat channel without noise, to isolate the effect of the distortion made only by the non-ideality of the PA. Since the compatibility condition is to be met, the RX has the structure exactly the same as Fig. 2 and the only parameter to be chosen is the one-tap equalization vector $\boldsymbol{s}_{\text{R}}$. We choose $\boldsymbol{s}_{\text{R}}$ to minimize the mean-squared error $\text{E}\{\|\boldsymbol{b} - \hat{\boldsymbol{b}}\|^2\}$ subject to zero inter-symbol interference, which is similar to the one-tap equalization vector in [32, Eq. (46)]. The only differences are that the derotation parameter in [32, Eq. (46)] is changed to $M/2$, and that the observation vector is pruned to have length M, in order to satisfy the compatibility condition. Although these metrics measured at the output of the PA are not easier to compute than the sampled-signal PAPR, they are the ultimate metrics that quantify the robustness of an input signal to the nonlinearity of the PA.

B. NUMERICAL RESULTS

In this subsection, numerical results are provided. For the DFT-spread OFDM with $L = M$, $\mathbf{1}_M$, $\boldsymbol{s}_{0.28}$, $\boldsymbol{s}_{\text{A-3}}$, and $\boldsymbol{s}_{\text{B-3}}$ are considered, where $\boldsymbol{s}_{\text{A-3}}$ and $\boldsymbol{s}_{\text{B-3}}$ are the 5-tap and 6-tap TD shaping filters in [8]. For the DFT-spread OFDM with $L > M$, the SRRC shaping vector $\boldsymbol{s}_{\text{SRRC}}$ in (31) and the proposed shaping vector $\boldsymbol{s}_{\text{T}}^*$ in (12a) are considered. These design examples satisfy the compatibility condition.

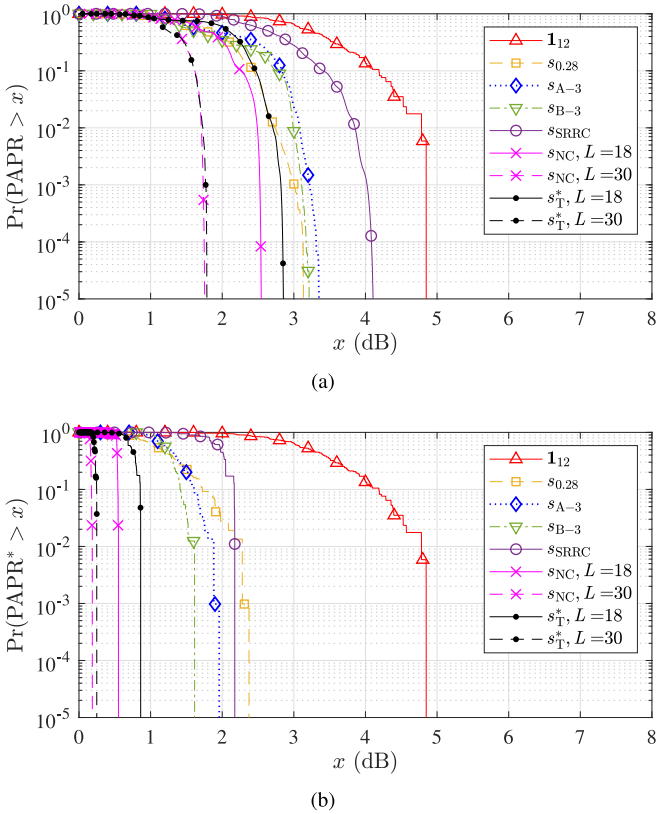

FIGURE 6. PAPR performance when $M = 12$: (a) CCDF of PAPR, (b) CCDF of PAPR*.

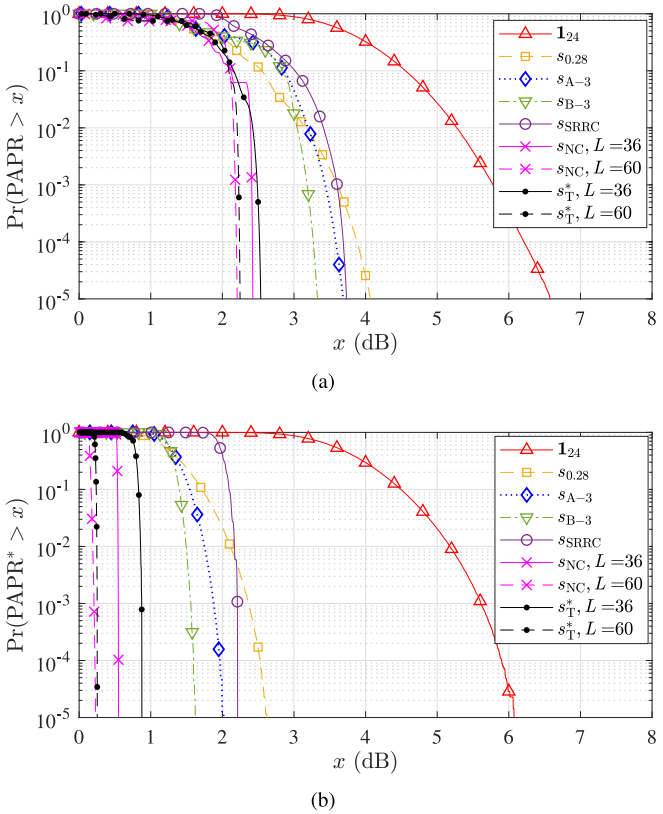

FIGURE 7. PAPR performance when $M = 24$: (a) CCDF of PAPR, (b) CCDF of PAPR*.

In addition, the numerically optimized design in [10] is also considered that does not satisfy the compatibility condition. The RX structure is the same for all designs except that the non-compatible one has extra constellation rotation in the RX.

Figs. 6 and 7 show the complementary cumulative distribution functions (CCDFs) of PAPR and PAPR* for $M = 12$ and $M = 24$, respectively. Figs. 6-(a) and 7-(a) show the approximate CCDFs, each of which is based on 2^{24} Monte-Carlo runs to generate three consecutive OFDM symbol periods, while Figs. 6-(b) and 7-(b) show the exact CCDFs. Since PAPR* is a discrete random variable and PAPR is also a discrete random variable in this simulation environment, the CCDFs are all piecewise constant functions. This is why some of the CCDF curves do not look smooth. For $M = 12$, the SRRC shaping vector has $L = 18$. The proposed design and the non-compatible one have $L = 18$ and 30. By comparing Fig. 6-(a) with Fig. 6-(b), we can see that PAPR of the CT signal $x(t)$ is a pessimistic predictor of the nonlinear robustness because even the proposed design has PAPR near 3 dB for $L = 18$ and near 2 dB for $L = 30$. All the design examples except $\mathbf{1}_{12}$ suffer from the PAPR degradation due to the phase discontinuity at the boundaries of OFDM symbols. Nevertheless, the proposed design outperforms all the conventional shaping vectors in terms both of PAPR and PAPR*. Moreover, if the envelope fluctuation at the boundaries are ignored because of its small energy, then

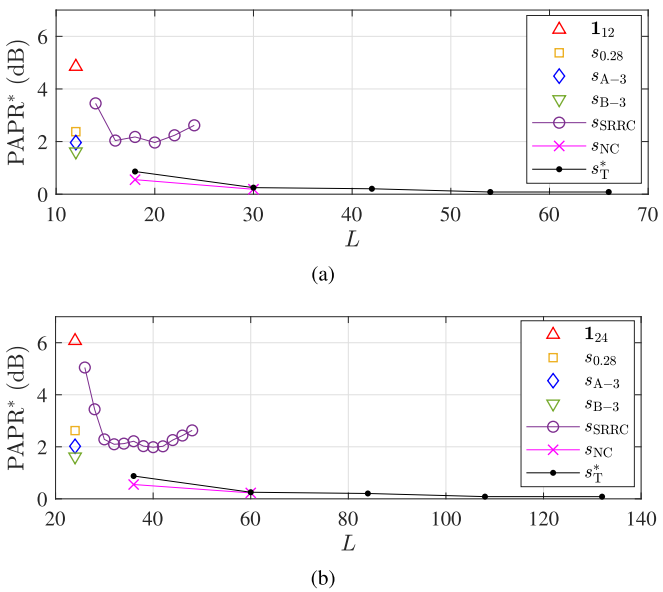

FIGURE 8. PAPR* performance at CCDF value 10^{-5} of the design examples: (a) $M = 12$ and (b) $M = 24$.

the proposed design generates an almost CE signal by achieving about 0.9 dB and 0.2 dB PAPR* at the CCDF value 10^{-5}, which is much smaller than the sampled-signal PAPR of other designs. On the contrary, the 6-tap and 3-tap TD filters in [8] and [9] achieve only 1.5 and 2.4 dB PAPR*,

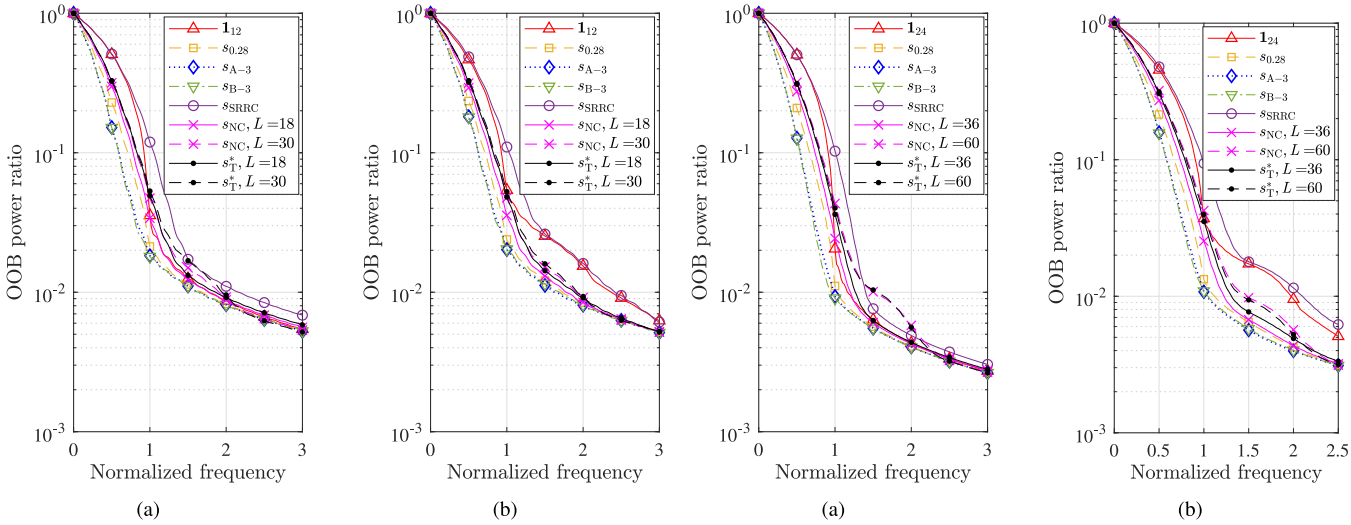

FIGURE 9. OOB power ratio of the design examples when $M = 12$: (a) ideal PA, and (b) nonlinear PA.

FIGURE 10. OOB power ratio of the design examples when $M = 24$: (a) ideal PA, and (b) nonlinear PA.

respectively. For $M = 24$, the SRRC shaping vector has $L = 36$ and the proposed one has $L = 36$ and 60. The comparison of Fig. 7-(a) with Fig. 7-(b) also shows similar PAPR degradation at the boundaries of OFDM symbols. However, if the envelope fluctuation at the boundaries are ignored, then the proposed design again achieves about 0.9 dB and 0.2 dB PAPR^* at the CCDF value 10^{-5}, and outperforms all the other designs. The non-compatible design $\boldsymbol{s}_{\mathrm{NC}}$ based on [10] has slightly less PAPR because the shaping vector and the rotation angle are both numerically optimized.

Fig. 8 shows PAPR^* of the proposed design, the non-compatible design, and the conventional ones at CCDF value 10^{-5} when $M = 12$ and $M = 24$. For the proposed design and the SRRC, it also shows PAPR^* as a function of L. It can be seen that PAPR^* of the proposed design approaches the PAPR of the ideal MSK signal as more excess sub-carriers are used. However, similar to the PAPR of a QPSK signal with an SRRC pulse [33], PAPR^* for the SRRC design does not always improve as more excess sub-carriers are used. Since Fig. 8 shows that PAPR^* is minimized when the roll-off factor β in (32) is around 0.5, we only choose the SRRC shaping vector with $(L - M)/M = 0.5$ in what follows.

Figs. 9 and 10 show the OOB power ratio as functions of normalized frequency. Here, the power ratio at a normalized frequency f_0 is defined as the signal power outside the frequency interval $[f_c - f_0 M\Delta f/2, f_c + f_0 M\Delta f/2]$, where f_c is the center frequency and Δf is sub-carrier spacing, divided by the total signal power. The adjacent channel leakage ratio and the spectrum mask [29], often used in the standards to regulate the amount of spectral regrowth can be obtained from this OOB power ratio. Figs. 9-(a) and 10-(a) show the power ratio when the ideal PA is used, while Figs. 9-(b) and 10-(b) show the power ratio when a nonlinear PA is used. These figures all include the effect of the abrupt changes of magnitude and phase at the boundaries between two OFDM symbols. Since $M \ll N$ is assumed, the energy of the magnitude and phase deviation at the boundaries is very small and consequently does not affect the OOB emission much. To characterize the input-output relation of the PA, we use a complex baseband model called the modified Rapp model and choose the parameters as specified in [34]. The OBO is set to 0.5 dB to make the model well approximate a solid-state PA operating in a highly nonlinear, but power-efficient, region.

Fig. 9 has $M = 12$ as in Fig. 6, so that the proposed shaping vector has $L = 18$ and 30, which correspond to the normalized frequencies 1.5 and 2.5, respectively, and the SRRC shaping vector has $L = 18$. By comparing Figs. 9-(a) and (b), it can be seen that the conventional designs with $\mathbf{1}_{12}$ and $\boldsymbol{s}_{\mathrm{SRRC}}$ suffer from spectral regrowth due to the nonlinearity of the PA, while the other designs have negligible spectral regrowth. The proposed design and the non-compatible design perform almost the same. The 99%-power bandwidth of the proposed design after the nonlinear PA is slightly worse than those of the conventional ones except $\mathbf{1}_{12}$ and $\boldsymbol{s}_{\mathrm{SRRC}}$. The slightly larger OOB emission of the proposed design in this case is due to the fact that the proposed shaping vector utilizes excess sub-carriers to reduce the envelope fluctuation significantly. When an ideal PA is used, the proposed design for $L = 18$ has almost the same 99%-power bandwidth as $\mathbf{1}_{12}$ and the proposed one for $L = 30$ has slightly larger 99%-power bandwidth. However, when the nonlinear PA is used, the proposed design has less 99%-power bandwidth, both for $L = 18$ and 30. Also note that, whether an ideal PA is used or not, the proposed design either for $L = 18$ or 30 has less 99%-power bandwidth than the SRRC shaping vector for $L = 18$. Fig. 9 has $M = 24$ as in Fig. 7, so that the proposed shaping vector has $L = 36$ and 60, which corresponds to the normalized frequencies

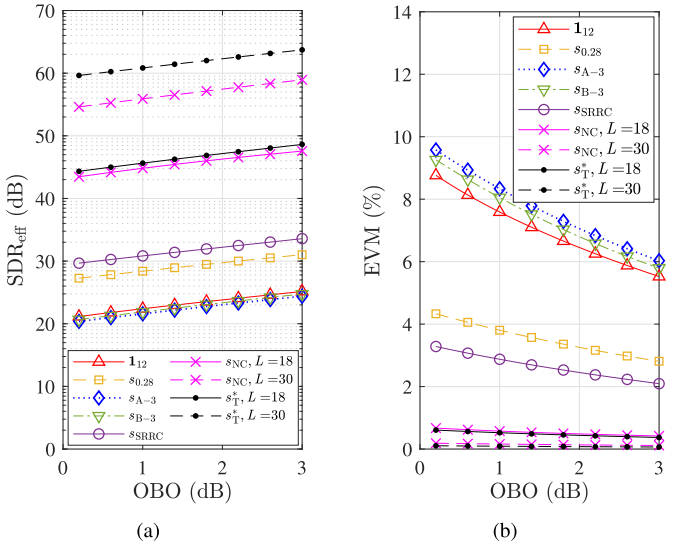

FIGURE 11. Effective SDR and EVM of the design examples as a function of OBO when $M = 12$: (a) effective SDR and (b) EVM.

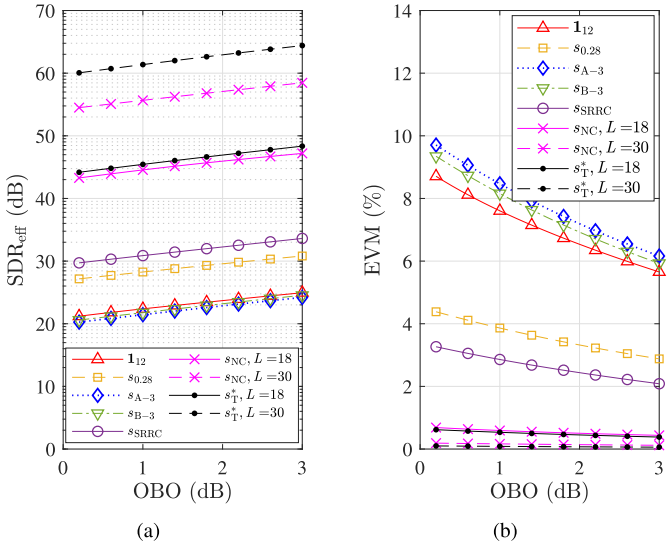

FIGURE 12. Effective SDR and EVM of the first data symbol of the design examples as a function of OBO when $M = 12$: (a) effective SDR and (b) EVM.

1.5 and 2.5, respectively, and the SRRC shaping vector has $L = 36$. Similar to Fig. 9, it can be seen that the conventional designs with $\mathbf{1}_{24}$ and $\boldsymbol{s}_{\text{SRRC}}$ suffer from spectral regrowth due to the nonlinearity of the PA, while the other designs have negligible spectral regrowth. When the nonlinear PA is used, the 99%-power bandwidth of the proposed design is slightly worse than those of the conventional ones except $\mathbf{1}_{12}$ and $\boldsymbol{s}_{\text{SRRC}}$, and better than $\mathbf{1}_{12}$ and $\boldsymbol{s}_{\text{SRRC}}$.

Fig. 11 shows the effective SDR and EVM of the design examples as a function of the OBO when $M = 12$. It can be seen that the proposed design outperforms all the other ones. In particular, the proposed design with $L = 18$ has greater than 41 dB effective SDR and less than 0.61% EVM, and the proposed design with $L = 30$ has greater than 59 dB effective SDR and less than 0.11% EVM for all OBO values in the range. Fig. 12 shows the effective SDR and EVM for the first $\pi/2$-BPSK symbol in each $\pi/2$-BPSK symbol vector in order to isolate and examine the effect of the phase discontinuity at the boundaries of OFDM symbols. It can be seen that all design examples have almost same the effective SDR and EVM as those in Fig. 11. As already mentioned, this is because the bandwidth of the transmitter is on the order of N times the sub-carrier spacing, which makes the envelope fluctuation at the boundaries have negligible power.

Unlike PAPR* that improves in the order of $\mathbf{1}_{12}$, $\boldsymbol{s}_{0.28}$, $\boldsymbol{s}_{\text{SRRC}}$, $\boldsymbol{s}_{\text{A-3}}$, $\boldsymbol{s}_{\text{B-3}}$, $\boldsymbol{s}_{\text{T}}^*$ for $L = 18$, $\boldsymbol{s}_{\text{NC}}$ for $L = 18$, $\boldsymbol{s}_{\text{T}}^*$ for $L = 30$, and $\boldsymbol{s}_{\text{NC}}$ for $L = 30$, the effective SDR and EVM in Figs. 11 and 12 improve in the order of $\boldsymbol{s}_{\text{A-3}}$, $\boldsymbol{s}_{\text{B-3}}$, $\mathbf{1}_{12}$, $\boldsymbol{s}_{0.28}$, $\boldsymbol{s}_{\text{SRRC}}$, $\boldsymbol{s}_{\text{NC}}$ for $L = 18$, $\boldsymbol{s}_{\text{T}}^*$ for $L = 18$, $\boldsymbol{s}_{\text{NC}}$ for $L = 30$, and $\boldsymbol{s}_{\text{T}}^*$ for $L = 30$. Notice that the designs with $\boldsymbol{s}_{\text{A-3}}$ and $\boldsymbol{s}_{\text{B-3}}$ have worse SDR and EVM performance than the DFT-spread OFDM without FDSS, even though they have better PAPR performance. Notice also that the non-compatible design has slightly worse SDR and EVM performance than the proposed one, even though it has slightly better PAPR performance. This is because the PAPR just roughly reflects the distribution of the signal envelope, which significantly affects the nonlinear distortion at the PA output. Fig. 13 shows the probability density function (PDF) of the signal envelope for $\mathbf{1}_{12}$, $\boldsymbol{s}_{0.28}$, $\boldsymbol{s}_{\text{A-3}}$, $\boldsymbol{s}_{\text{B-3}}$, $\boldsymbol{s}_{\text{NC}}$ for $L = 18$, $\boldsymbol{s}_{\text{T}}^*$ for $L = 18$, $\boldsymbol{s}_{\text{NC}}$ for $L = 30$, and $\boldsymbol{s}_{\text{T}}^*$ for $L = 30$, when $M = 12$. Similar PDFs can be obtained when $M = 24$. After the power of the PA input is normalized, the absolute value $|x_n|$ of each entry of all 2^{12} OFDM symbol vectors $\boldsymbol{x}$ are taken and the PDF is computed with bin interval 0.01. Note that $\mathbf{1}_{12}$ and $\boldsymbol{s}_{\text{T}}^*$ exhibit uni-modal envelope distributions, while $\boldsymbol{s}_{\text{A-3}}$ and $\boldsymbol{s}_{\text{B-3}}$ exhibit bi-modal envelope distributions. Since the input-output relation of the PA deviates more from linearity as the input power increases, $\boldsymbol{s}_{\text{A-3}}$ and $\boldsymbol{s}_{\text{B-3}}$ result in worse SDR and EVM performance than $\mathbf{1}_{12}$, even though they have much smaller PAPR* or, equivalently, peak value of $|x_n|$. The proposed design outperforms the other compatible designs because it has not only a smaller peak value but also a uni-modal distribution. Unfortunately, sometimes the PDFs are very narrow and indistinguishable, as exemplified by Figs. 13-(e) and (f), and by Figs. 13-(g) and (h). Nevertheless, Figs. 11 and 12 show that the proposed design $\boldsymbol{s}_{\text{T}}^*$ slightly outperforms the corresponding non-compatible design $\boldsymbol{s}_{\text{NC}}$ in the SDR and EVM.

As mentioned in the Introduction, the non-compatible design in [10] is proposed for future wireless systems that allows extra constellation rotation in the RX. This method needs the shaping vector to be found through numerical search and the rotation angle to be adjusted whenever a new combination of the numbers of $\pi/2$-BPSK symbols and excess sub-carriers is given. On the contrary, the proposed design is not only compatible with the current standards but also requires no numerical optimization. Moreover, the above numerical results show that the proposed design

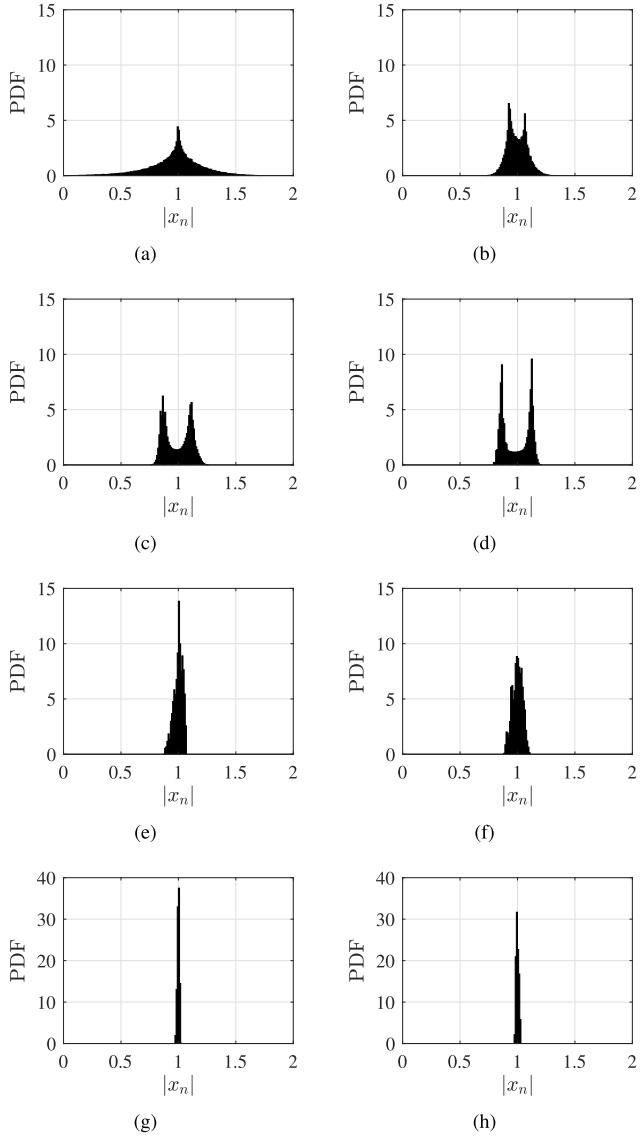

FIGURE 13. PDF of the absolute value $|x_n|$ of OFDM symbol vector x: (a) 1_{12}, (b) $s_{0.28}$, (c) s_{A-3}, (d) s_{B-3}, (e) s_{NC} for $L = 18$, (f) s_T^* for $L = 18$, (g) s_{NC} for $L = 30$, and (h) s_T^* for $L = 30$.

achieves slightly better performance than the non-compatible numerically optimized design in [10].

Fig. 14 compares the effective SDR and EVM of the proposed design and its relaxed version when $M = 12$. The relaxation is made by removing the compatibility condition (22) and allow an extra constellation rotation in the RX as similarly done in [10]. The shaping vector now has the lth element given by

$$\tilde{s}_{\mathrm{T},l} \triangleq \mathrm{sinc}\left(\frac{-2l + L^* + 1}{M} + \frac{1}{2}\right) + \mathrm{sinc}\left(\frac{2l - L^* - 1}{M} + \frac{1}{2}\right), \tag{37a}$$

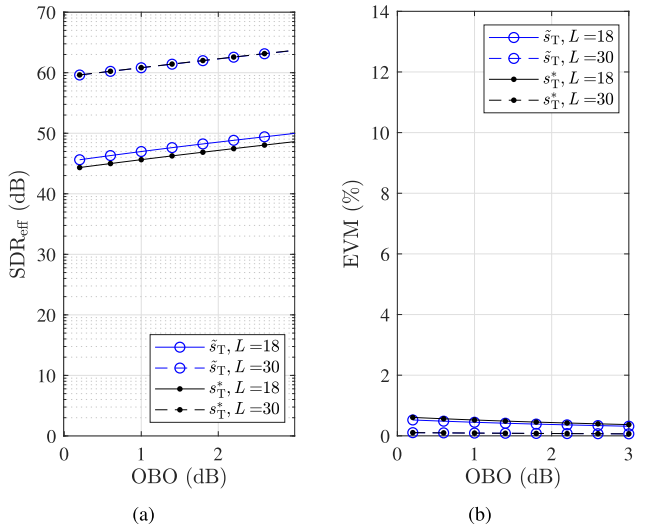

FIGURE 14. Effective SDR and EVM of the proposed design and its relaxed version as a function of OBO when $M = 12$: (a) effective SDR and (b) EVM.

for $l = 1, 2, \ldots, L^*$, and the extra rotation angle in the TX is now given by

$$\phi_{\mathrm{T}} \triangleq \mathrm{mod}\left(\frac{L^* - M - 1}{M}\pi, 2\pi\right), \tag{37b}$$

where L^* is given by (12b). Notice that, unlike $\boldsymbol{s}_{\mathrm{T}}^*$ that is symmetric with an odd effective length, the shaping vector $\tilde{\boldsymbol{s}}_{\mathrm{T}}$ is symmetric with an even effective length. The extra constellation rotation in the RX needs to be introduced between the fifth and sixth blocks of Fig. 2, which changes the input to the sixth block from $\hat{\boldsymbol{d}}$ to $\boldsymbol{R}(\phi_{\mathrm{R}})\hat{\boldsymbol{d}}$, where

$$\phi_{\mathrm{R}} \triangleq \frac{\pi}{M}. \tag{38}$$

The extra constellation rotation ϕ^* in the TX of the proposed design is required to place the first entry of the length-L^* DFT-spreader output not at the $(K+1)$th sub-carrier location but at the $(K_{\mathrm{T}}+1)$th sub-carrier location. However, this extra rotation angle alone cannot satisfy the I-Q orthogonality condition. When the shaping vector has the real symmetry with an even effective length as exemplified by $\tilde{\boldsymbol{s}}_{\mathrm{T}}$ of the relaxed design, it can be easily shown that the extra rotation angle ϕ^* still satisfies the compatibility condition but not the I-Q orthogonality condition. For $\tilde{\boldsymbol{s}}_{\mathrm{T}}$ to satisfy the I-Q orthogonality, the extra rotation angle in the TX must be changed from ϕ^* to ϕ_{T} and there must be an extra rotation ϕ_{R} in the RX. In this sense, it can be summarized that the compatibility condition is satisfied alone by the extra rotation angle ϕ^* but the I-Q orthogonality condition is jointly satisfied the angle and the symmetry with an odd effective length. As Fig. 14 shows, there is almost no performance gain or loss by removing the compatibility condition. Although not provided here, it can also be shown that there is almost no performance gain or loss in terms of the OOB emission and the PAPR. Hence, the proposed design has no penalty for satisfying the compatibility condition.

V. CONCLUSION

In this paper, we have shown that an almost CE signal can be generated for the DFT-spread OFDM of $\pi/2$-BPSK symbols. Specifically, the combinations of an MSK pulse-like shaping vector and an extra constellation rotation are proposed, which not only satisfy both the orthogonality and compatibility conditions, but also do not require any numerical search for near-optimal shaping vectors. The performance of the proposed design is analyzed at the input and output of a highly nonlinear PA. With a negligible increase in OOB emission, the proposed CPM for the DFT-spread OFDM significantly outperforms the conventional modulation in terms of the PAPR at the PA input and the effective SDR and EVM at the PA output. Because the proposed design has excellent effective SDR and EVM when the nonlinearity of the PA is solely taken into account, further research is warranted to investigate the effects of other non-idealities of RF components such as phase noise, filter distortion, I/Q imbalance, etc.

REFERENCES

[1] "IMT vision—Framework and overall objectives of the future development of IMT for 2020 and beyond," Int. Telecommun. Union, Geneva, Switzerland, ITU-Recommendation M.2083-0, Sep. 2015.

[2] C. Bockelmann *et al.*, "Massive machine-type communications in 5G: Physical and MAC-layer solutions," *IEEE Commun. Mag.*, vol. 54, no. 9, pp. 59–65, Sep. 2016.

[3] S. K. Sharma and X. Wang, "Toward massive machine type communications in ultra-dense cellular IoT networks: Current issues and machine learning-assisted solutions," *IEEE Commun. Surveys Tuts.*, vol. 22, no. 1, pp. 426–471, 1st Quart., 2020.

[4] C. Yu, L. Yu, Y. Wu, Y. He, and Q. Lu, "Uplink scheduling and link adaptation for narrowband Internet of Things systems," *IEEE Access*, vol. 5, pp. 1724–1734, 2017.

[5] S. C. Thompson, A. U. Ahmed, J. G. Proakis, J. R. Zeidler, and M. J. Geile, "Constant envelope OFDM," *IEEE Trans. Commun.*, vol. 56, no. 8, pp. 1300–1312, Aug. 2008.

[6] V. Jungnickel and L. Grobe, "Method and apparatus for transmitting a signal," U.S. Patent 10 103 921 B2, Oct. 16, 2018.

[7] M. P. Wylie-Green, E. Perrins, and T. Svensson, "Introduction to CPM-SC-FDMA: A novel multiple-access power-efficient transmission scheme," *IEEE Trans. Commun.*, vol. 59, no. 7, pp. 1904–1915, Jul. 2011.

[8] K. Kuchi, "Partial response DFT-precoded-OFDM modulation," *Eur. Trans. Telecommun.*, vol. 23, no. 7, pp. 632–645, 2012.

[9] *Additional Simulation Results on Low PAPR RS*, 3GPP TSG RAN WG1 Meeting Ad-Hoc Meeting 1901, R1-1901117, Ericsson, Taipei, Taiwan, Jan. 2019.

[10] J. Kim, Y. H. Yun, C. Kim, and J. H. Cho, "Minimization of PAPR for DFT-spread OFDM with BPSK symbols," *IEEE Trans. Veh. Technol.*, vol. 67, no. 12, pp. 11746–11758, Dec. 2018.

[11] J. G. Proakis and M. Salehi, *Digital Communications*, 5th ed. New York, NY, USA: McGraw-Hill, 2008.

[12] S. Haykin and M. Moher, *Communication Systems*, 5th ed. Hoboken, NJ, USA: Wiley, 2009.

[13] *Technical Specification Group Radio Access Network; Evolved Universal Terrestrial Radio Access (E-UTRA); Physical Channels and Modulation, Release 15*, 3GPP Standard TS 36.211 v15.5.0, Mar. 2019.

[14] *Technical Specification Group Radio Access Network; NR; Physical Channels and Modulation, Release 15*, 3GPP Standard TS 38.211 v15.6.0, Jun. 2019.

[15] H. Ochiai, "An analysis of band-limited communication systems from amplifier efficiency and distortion perspective," *IEEE Trans. Commun.*, vol. 61, no. 4, pp. 1460–1472, Apr. 2013.

[16] *Way Forward on Low PAPR Modulation in NR*, 3GPP TSG-RAN WG1 Meeting #86bis, R1-1610904, Samsung, Qualcomm, Intel, Vodafone, AT&T, MediaTek, KDDI, InterDigital, IITH, IITM, Tejas Netw., Reliance-Jio, CEWiT, Nat. Instrum., Lisbon, Portugal, Oct. 2016.

[17] P. A. Laurent, "Exact and approximate construction of digital phase modulations by superposition of amplitude modulated pulses (AMP)," *IEEE Trans. Commun.*, vol. 34, no. 2, pp. 150–160, Feb. 1986.

[18] U. Mengali and M. Morelli, "Decomposition of M-ary CPM signals into PAM waveforms," *IEEE Trans. Inf. Theory*, vol. 41, no. 5, pp. 1265–1275, Sep. 1995.

[19] X. Huang and Y. Li, "The PAM decomposition of CPM signals with integer modulation index," *IEEE Trans. Commun.*, vol. 51, no. 4, pp. 543–546, Apr. 2003.

[20] E. Perrins and M. Rice, "PAM decomposition of M-ary multi-h CPM," *IEEE Trans. Commun.*, vol. 53, no. 12, pp. 2065–2075, Dec. 2005.

[21] *Narrow Band OFDMA-Tone-Phase-Shift Keying Modulation*, 3GPP TSG GERAN #64, Tdoc GP-140842, Qualcomm, San Francisco, CA, USA, Nov. 2014.

[22] S. B. Slimane, "Reducing the peak-to-average power ratio of OFDM signals through precoding," *IEEE Trans. Veh. Technol.*, vol. 56, no. 2, pp. 686–695, Mar. 2007.

[23] A. Lapidoth, *A Foundation in Digital Communication*, 2nd ed. New York, NY, USA: Cambridge Univ. Press, 2017.

[24] V. Tervo, A. Tölli, J. Karjalainen, and T. Matsumoto, "PAPR constrained power allocation for iterative frequency domain multiuser SIMO detector," in *Proc. IEEE Int. Conf. Commun. (ICC)*, Sydney, NSW, Australia, Jun. 2014, pp. 4735–4740.

[25] J. Ji, G. Ren, and H. Zhang, "PAPR reduction in coded SC-FDMA systems via introducing few bit errors," *IEEE Commun. Lett.*, vol. 18, no. 7, pp. 1258–1261, Jul. 2014.

[26] C. H. G. Yuen and B. Farhang-Boroujeny, "Analysis of the optimum precoder in SC-FDMA," *IEEE Trans. Wireless Commun.*, vol. 11, no. 11, pp. 4096–4107, Nov. 2012.

[27] R. Bai, Z. Wang, R. Jiang, and J. Cheng, "Interleaved DFT-spread layered/enhanced ACO-OFDM for intensity-modulated direct-detection systems," *J. Lightw. Technol.*, vol. 36, no. 20, pp. 4713–4722, Oct. 15, 2018.

[28] H. G. Myung, J. Lim, and D. J. Goodman, "Peak-to-average power ratio of single carrier FDMA signals with pulse shaping," in *Proc. IEEE 17th Int. Symp. Pers. Indoor Mobile Radio Commun. (PIMRC)*, Helsinki, Finland, Sep. 2006, pp. 1–5.

[29] *Technical Specification Group Radio Access Network; NR; User Equipment (UE) Radio Transmission and Reception; Part 1: Range 1 Standalone, Release 16*, 3GPP Standard TS 38.101-1 v16.6.0, Dec. 2020.

[30] Z. Feng, J. Rui, S. Jing-Lu, and Z. Xin, "Analysis on the definition consistency problem of EVM measurement and its solution," *IEEE Trans. Instrum. Meas.*, vol. 69, no. 2, pp. 528–532, Feb. 2020.

[31] D. A. Humphreys and R. T. Dickerson, "Traceable measurement of error vector magnitude (EVM) in WCDMA signals," in *Proc. Int. Waveform Diversity Design Conf.*, Pisa, Italy, Jun. 2007, pp. 270–274.

[32] J. Choi, J. Kim, J. H. Cho, and J. S. Lehnert, "Widely-linear nyquist criteria for DFT-spread OFDM of constellation-rotated PAM symbols," *IEEE Trans. Commun.*, vol. 69, no. 5, pp. 2909–2922, May 2021.

[33] S. Daumont, B. Rihawi, and Y. Lout, "Root-raised cosine filter influences on PAPR distribution of single carrier signals," in *Proc. 3rd Int. Symp. Commun. Control Signal Process.*, Saint Julian's, Malta, Mar. 2008, pp. 841–845.

[34] *TGay Evaluation Methodology, Sec. 2.2.3*, IEEE document P802.11-15/0866r4, IEEE, Piscataway, NJ, USA, Jan. 2016.

JEONGHOON CHOI received the B.S. degree in electrical engineering from the Pohang University of Science and Technology, Pohang, South Korea, in 2014, where he is currently pursuing the Ph.D. degree. His research interests include mobile communications and waveform design.

JOON HO CHO (Member, IEEE) received the B.S. degree (*summa cum laude*) in electrical engineering from Seoul National University, Seoul, South Korea, in 1995, and the M.S.E.E. and Ph.D. degrees in electrical and computer engineering from Purdue University, West Lafayette, IN, USA, in 1997 and 2001, respectively.

From 2001 to 2004, he was with the University of Massachusetts at Amherst as an Assistant Professor. Since July 2004, he has been with the Pohang University of Science and Technology (POSTECH), Pohang, South Korea, where he is currently an Associate Professor with the Department of Electrical Engineering. His research interests include waveform design, multiuser communications, MIMO signal processing, channel measurement and modeling, and information theory.

Dr. Cho served as an Associate Editor for the IEEE TRANSACTIONS ON VEHICULAR TECHNOLOGY and served as the Vice President for Admissions and Student Affairs of POSTECH.

JAMES S. LEHNERT (Fellow, IEEE) received the B.S. (Highest Hons.), M.S., and Ph.D. degrees in electrical engineering from the University of Illinois at Urbana–Champaign in 1978, 1981, and 1984, respectively.

From 1978 to 1984, he was a Research Assistant with the Coordinated Science Laboratory, University of Illinois at Urbana–Champaign, Urbana, IL, USA. He has held summer positions with the Data Systems Research Laboratory, Motorola Communications, Schaumburg, IL, USA, and the Advanced Technology Department, Harris Corporation, Melbourne, FL, USA. He is currently a Professor with the School of Electrical and Computer Engineering, Purdue University, West Lafayette, IN, USA, where he became a Purdue University Faculty Scholar in 2003. His current research work is in communication and information theory with emphasis on spread-spectrum and adaptive communications.

Prof. Lehnert received the IEEE Military Communications Conference Award for Technical Achievement in 2009. He has served as an Editor for Spread Spectrum for the IEEE TRANSACTIONS ON COMMUNICATIONS and as a Guest Editor for the IEEE JOURNAL ON SELECTED AREAS IN COMMUNICATIONS. He was a University of Illinois Fellow from 1978 to 1979, and an IBM Pre-Doctoral Fellow from 1982 to 1984.